

RESEARCH ARTICLE | JUNE 01 1992

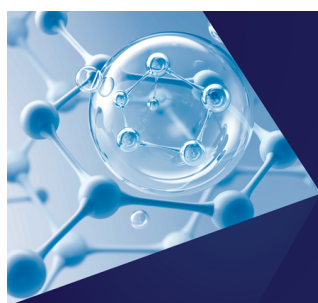
Precursor and overlayer structural effects in the interaction of CO with Ni(110)

Michael A. DeAngelis; Andrew M. Glines; A. Brad Anton



J. Chem. Phys. 96, 8582–8594 (1992)

<https://doi.org/10.1063/1.462311>



The Journal of Chemical Physics
**Special Topics Open
for Submissions**

[Learn More](#)

Precursor and overlayer structural effects in the interaction of CO with Ni(110)

Michael A. DeAngelis, Andrew M. Glines, and A. Brad Anton
School of Chemical Engineering, Cornell University, Ithaca, New York 14853-5201

(Received 29 January 1992; accepted 28 February 1992)

We present isothermal measurements of CO adsorption and desorption rates on Ni(110) that reveal clearly the participation of a precursor state in both processes at all coverages. Accounting for its effect allows activation energies and preexponential factors to be determined that are specific to the coverage regimes where $c(8 \times 2)$, $c(4 \times 2)$, and (2×1) ordered structures are known to form at low temperatures. The preexponential factors include a significant contribution attributable to relaxation of the adsorbed layer from one structure to another as desorption proceeds, and the relaxation process is also manifested in the relationship between measured activation energies and integral heats of adsorption. The results have general implications for adsorption systems involving series of ordered overlayers.

I. INTRODUCTION

Adsorption and desorption *kinetics* play a critical role in defining the relationship between processing conditions—temperature, reactant pressures, etc.—and overall rates for reactions at gas/solid interfaces. Lately, many fundamental studies have focused specifically on the *dynamics* of adsorption and desorption using state-resolved measurements to identify the individual roles of translational, rotational, and vibrational degrees of freedom.¹ In principle, the two are intimately related. The participation of various internal degrees of freedom is reflected in the magnitudes of preexponential factors for kinetic rate constants, and the dynamical energy barriers evident in state-resolved measurements are related to chemical activation energies.² Dynamics investigations are often conducted under conditions far removed from thermal equilibrium, however, and tend to probe only limited portions of the multidimensional adsorbate/adsorbent potential energy surface. Consequently, the mechanistic pathways and energy barriers they identify may not be relevant to thermally activated reactions. Significant incentives remain to investigate the kinetics of adsorption and desorption under conditions at or approaching thermal equilibrium, where the Boltzmann energy distribution tends naturally to select the multidimensional pathways of minimum energy.³ Such investigations not only aid the development of accurate kinetic models for heterogeneous reactions, but they provide indispensable input to currently evolving Monte Carlo and molecular dynamics simulations of equilibrium chemisorption behavior.⁴

Mechanistic aspects of the adsorption and desorption process relevant to thermal equilibrium are evidenced most clearly in the variation of their rates with surface coverage and temperature.⁵ We demonstrate here that many aspects of the desorption mechanism can be elucidated by analyzing the coverage dependence of its rate at constant temperature, as determined with a qualitative refinement of a traditional technique, temperature-programmed desorption (TPD).⁶ Our results for the particular case of CO/Ni(110) verify the participation of a mobile, weakly bound “precursor” to site-specific chemisorption at all coverages, and they show a

sharp transition, dependent on the coverage and structure of the adsorbed layer, between two limiting behaviors expected for this type of mechanism. Measurements of the coverage-dependent adsorption rate under conditions approaching thermal equilibrium are fully consistent with this interpretation.

The concept of mobile chemisorption precursors has a rich history in the surface science literature, beginning with Langmuir's insightful postulate of their existence.⁷ The precursor forms as a result of long-range, nonorientative dispersion forces and therefore can be thought of as a van der Waals complex of the adsorbate-adsorbent system. These forces cause adsorbing or desorbing molecules to “trap” temporarily in a shallow minimum of the adsorbate/adsorbent potential, typically a few kcal/mol deep, 3–5 Å from the surface plane and outside the range of the deep and strongly orientative well responsible for site-specific chemisorption (cf. Fig. 1).⁸ Surface science vernacular distinguishes be-

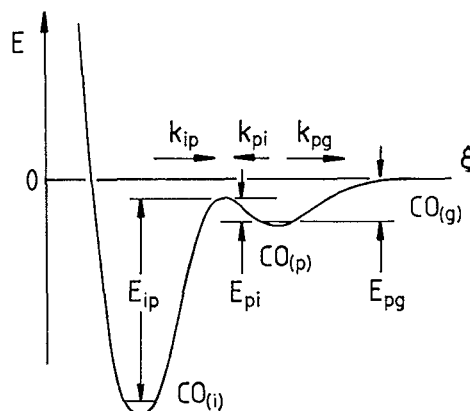


FIG. 1. Diagram of potential energy E vs reaction coordinate ξ (Ref. 8) for precursor-mediated interaction of $\text{CO}_{(g)}$ (gas phase) with $\text{CO}_{(i)}$ (chemisorbed state i). E_{ip} and k_{ip} are the activation energy and rate constant for formation of $\text{CO}_{(p)}$ (precursor) from $\text{CO}_{(i)}$, E_{pi} and k_{pi} are the same quantities for the reverse reaction, and E_{pg} and k_{pg} are the same quantities for formation of $\text{CO}_{(g)}$ from $\text{CO}_{(p)}$.

tween "intrinsic precursors" that exist over vacant adsorption sites and "extrinsic precursors" that exist over occupied sites,⁹ although a distinction between these is rarely observed in practice.¹⁰ The existence and shape of the precursor well has important implications for the dynamics and kinetics of surface reactions, motivating intense experimental and theoretical scrutiny of surface reactions thought to be mediated by mobile precursors.¹⁰

The interaction of CO with Ni(110) is a prototypical system that has been characterized with a variety of analytical techniques. Low-energy electron diffraction (LEED) measurements show three ordered structures being formed sequentially as Ni(110) is exposed to CO at 130 K,¹¹ as depicted in Fig. 2. At coverages below $\vartheta = 0.625$ ml,¹² regions of $c(8 \times 2)$ symmetry are evident, and adding molecules to these causes islands of $c(4 \times 2)$ symmetry to grow at the expense of the $c(8 \times 2)$ structure until the $c(4 \times 2)$ overlayer is complete at $\vartheta = 0.75$ ml. Subsequent exposure causes the $c(4 \times 2)$ overlayer to be converted to the (2×1) overlayer by a similar island-growth mechanism. At saturation, the coverage of the ideal (2×1) overlayer is $\vartheta = 1.0$ ml,¹¹ but absolute coverage measurements suggest that disorder, kinetically "frozen" into the overlayer during adsorption, limits the saturation coverage to $\vartheta = 0.92 \pm 0.04$ ml at low temperature.¹³ The vibrational structure of the (2×1) overlayer has been characterized elegantly by recent electron-energy-loss spectroscopy (EELS) measurements.¹⁴ TPD measurements show a sharp peak at ~ 360 K associated with dissolution of the (2×1) structure and a broad, asymmetric peak near 440 K associated with sequential desorption from the $c(4 \times 2)$ and $c(8 \times 2)$ structures.^{11,15,16} Measurements of the adsorption probability at low temperature implicate the participation of a precursor state,¹¹ but it has not been characterized, and its relevance to desorption at higher temperatures has not been assessed.

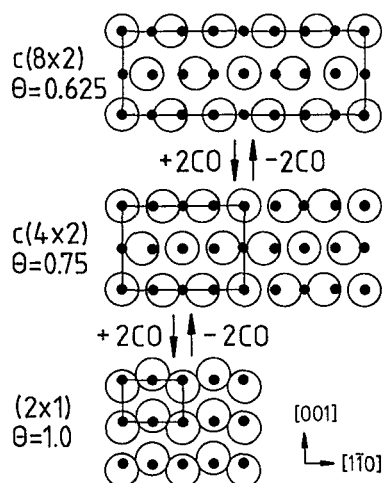


FIG. 2. The depiction of the reversible reactions that convert a $c(8 \times 2)$ unit cell to two unit cells of $c(4 \times 2)$ symmetry and a $c(4 \times 2)$ unit cell to four unit cells of (2×1) symmetry. The overlayer structures are those suggested in Ref. 11 on the basis of LEED measurements. The open circles represent adsorbed CO molecules, the solid circles represent nickel surface atoms, and the solid lines identify the unit cells for each structure.

II. EXPERIMENTAL DETAILS

The experiments we describe were performed in a two-chamber ultrahigh vacuum system with a base pressure of 2×10^{-10} Torr, as measured with a nude, uncalibrated ion gauge. One chamber contains the liquid nitrogen-cooled sample holder and is evacuated by a 400 ℓ /s ion pump and a titanium sublimation pump. The second chamber houses a quadrupole mass spectrometer with provisions for ion counting and is evacuated by a turbomolecular and a titanium sublimation pump.¹⁷ The two chambers are connected by a 3 mm orifice, positioned to give line of sight from the ionizer of the mass spectrometer to a 6 mm circle on the face of the sample. The liquid nitrogen-cooled sublimation pump in the mass spectrometer chamber is annular in shape and completely surrounds the ionizer, giving a pumping speed in this region on the order of several hundred liters per second and ensuring that the dominant contribution to the measured signal is the direct flux from the sample. The Ni(110) surface, prepared with standard techniques, is cleaned as required with cycles of Ar^+ ion bombardment and high temperature annealing. Its temperature is monitored with a thermocouple spot welded to the rear face near the center. The thermocouple and a d.c. power supply for direct, resistive heating are interfaced to a personal computer, and together they constitute a digital feedforward/feedback control system that allows the temperature to be programmed to approximate various time-dependent functions including linear ramps, step functions, and periodic sine waves.¹⁸ The desorption data presented here were collected with the step-function program, with which the sample's temperature can be increased by 80 K within 5 s without overshoot. This allows the desorption rate to be measured under isothermal conditions, revealing more clearly its dependence on coverage and obviating the problem of temperature nonuniformity that can limit the precision of traditional TPD.¹⁹

A typical desorption measurement begins with exposure of the sample to CO at 80 K to prepare a saturated adlayer and annealing for 30 s at 200 K to ensure its order prior to desorption. The signal (ion counts at $m/e = 28$ amu) is collected over fixed intervals of time while the temperature is ramped to a starting point approximately 80 K below the desired temperature for data collection, and a rapid step to the final temperature (± 0.1 K) is made, after which the signal decays as the surface empties. In some cases, two sequential 80 K steps are used, since for low temperatures the desorption rate decays to a negligible level well before the surface has emptied. In every case, the measurement ends with a ramp to high temperature to clear all CO from the surface for accurate determination of the initial surface coverage. Ion counts are summed over channels of 0.10 s width, significantly narrower than is required to obtain adequate time resolution, to avoid saturation of the 16 bit counter, since peak intensities exceed 2×10^5 counts/s. The raw data are corrected for the $1.25 \mu\text{s}/\text{count}$ dead time of the signal processing circuitry,²⁰ the constant background is subtracted, and the resulting pure desorption signal, assumed to include only molecules that have come directly from the sample without scattering from the chamber walls, is corrected for the density-dependent sensitivity of the mass spectrom-

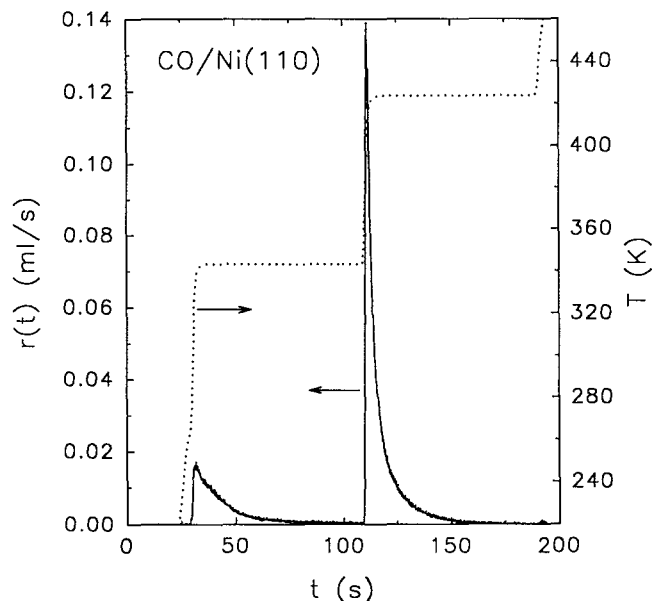


FIG. 3. Results of a typical measurement of the desorption rate as a function of time for a two-step temperature program.

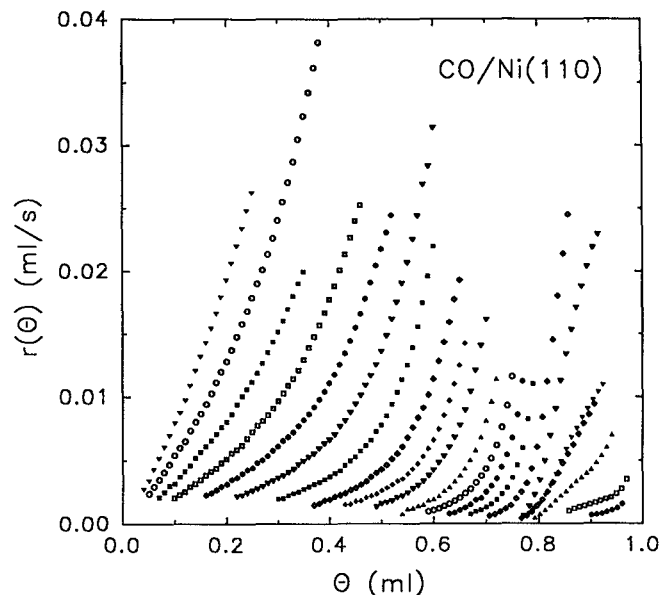


FIG. 4. Desorption rate $r(\vartheta)$ vs coverage ϑ determined from data such as those of Fig. 3. The temperatures for the curves span in approximately 5 K increments over a range from 323 K at the lower right to 423 K at the upper left.

eter by assuming the average kinetic energy of the desorbing molecules is proportional to the surface temperature.²¹ With these corrections, the integral signal intensity for the entire measurement, which should be proportional to the initial surface coverage, is reproducible for repeated experiments to within $\pm 2\%$. The net result of this procedure for a typical measurement is shown in Fig. 3. The dynamic range of the isothermal portions of the measurement is limited at the maximum by the time required to accomplish the temperature change and at the minimum by the steady-state background signal at $m/e = 28$ amu. Because of these constraints, the isothermal rate spans only a range from 0.001 to 0.04 ml/s. Since the data are necessarily collected over short time intervals, the isothermal portions are "smoothed" to improve the statistics with a digital filter that approximates a Gaussian of 5 s width. Finally, the integral of the signal from each time interval to $t \rightarrow \infty$ is used to convert the final data of desorption rate $r(t)$ vs t for each temperature to $r(\vartheta)$ vs ϑ , resulting in the set of curves shown in Fig. 4 for temperatures from 323 to 423 K.

For optimum comparison to the desorption data, adsorption rates should be measured by exposing the surface to a spatially uniform flux of CO with the gas and surface temperatures equal and similar to those used in the desorption measurements, a circumstance that is difficult to realize in an ultrahigh vacuum chamber. To approximate this, the chamber is backfilled with CO through a calibrated orifice to a uniform pressure near 2×10^{-8} Torr, and the flux of CO reflected from the initially clean surface is detected as a function of time with the mass spectrometer in line-of-sight geometry, giving for a typical case the curve $Q(t)$ shown in Fig. 5. A second measurement is made that begins with a CO-saturated surface, giving the curve $P(t)$ of Fig. 5. The adsorption rate is proportional to $P(t) - Q(t)$, and this func-

tion can be corrected, smoothed, and integrated as described for the desorption measurements to yield a curve of relative adsorption probability $S(\vartheta)/S(\vartheta = 0)$ vs ϑ .²² The subtraction and division operations degrade the statistics somewhat and may introduce a small artifact that causes a spurious, but gradual decrease of $S(\vartheta)$ with increasing ϑ ; nonetheless,

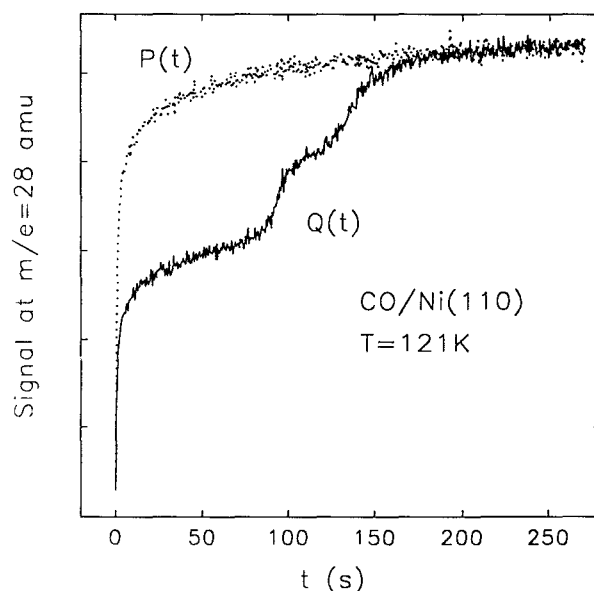


FIG. 5. Typical data from which the adsorption probability as a function of coverage is determined (Ref. 22). Both curves are $m/e = 28$ amu signals emitted from the surface as the chamber is filled with CO at a constant rate through a calibrated orifice. The surface is clean when the measurement of $Q(t)$ begins and saturated with CO when the measurement of $P(t)$ begins.

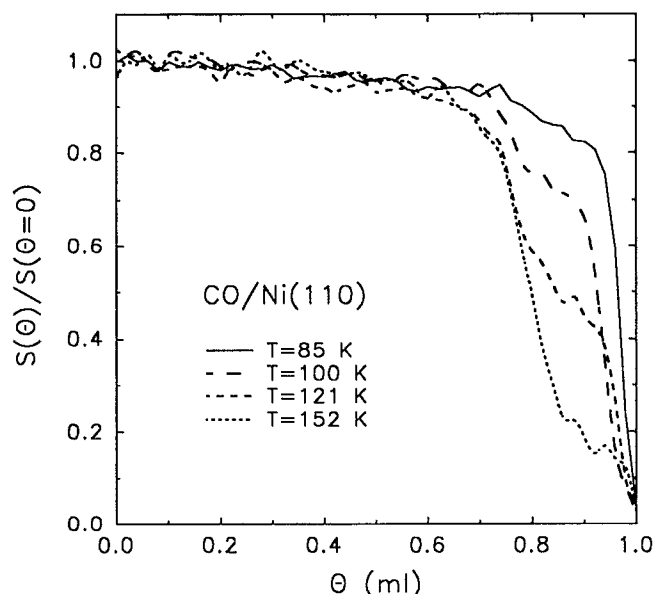


FIG. 6. Relative adsorption probability $S(\vartheta)/S(\vartheta=0)$ vs coverage ϑ determined from data such as those of Fig. 5 for $T = 85, 101, 121$, and 152 K.

the curves reveal very clearly any abrupt changes in $S(\vartheta)$ that may result from coverage-dependent transitions in the adsorption mechanism.²² Results of this procedure for surface temperatures of 85, 101, 121, and 152 K, where desorption is negligibly slow, are shown in Fig. 6. Since the gas temperature is 300 K, thermal equilibrium is not rigorously attained in these measurements, but nonequilibrium effects should be negligible in this context.

III. RESULTS

The shapes of the curves in Figs. 4 and 6 guide us in developing an adsorption/desorption mechanism and kinetic model, the efficacy of which will be demonstrated as we proceed to compare it to the data. Note first the systematic upward curvature of $r(\vartheta)$ and the near constancy of $S(\vartheta)$ for coverages less than about 0.8 ml; considered together, these implicate a precursor mechanism such as that described by the one-dimensional potential energy function of Fig. 1.⁹ Note also the abrupt change in the behavior for coverages above about 0.8 ml, where the $c(4 \times 2)$ and (2×1) overlayers coexist. The $r(\vartheta)$ curves appear to be nearly straight lines and $S(\vartheta)$ falls off toward zero. There is no *a priori* reason why the precursor should cease to exist in this coverage range, so we attribute this transition to a coverage-dependent change in the relative rates at which precursor molecules desorb to the gas phase or return to chemisorption sites. These considerations lead us to extend the traditional precursor model to include rate parameters that are specific to the state of local order in the chemisorbed layer.

Assume that three *distinct* and *local* chemisorption "environments" exist for CO on the Ni(110) surface, corre-

sponding to the coverage regimes for each of the three structures shown in Fig. 2. Let ϑ_1 be the coverage of $c(8 \times 2)$ sites, ϑ_2 be that of $c(4 \times 2)$ sites, and ϑ_3 be that of (2×1) sites, with ϑ_{1s} , ϑ_{2s} , and ϑ_{3s} as their respective saturation coverages, and let ϑ_v be the coverage of vacant sites. At this point, we assume the saturation coverages are unknown; we will estimate them from the shape of the desorption rate curves for comparison to the "ideal" values determined from LEED studies¹¹ (*vide infra*). Assume also that adsorbed molecules move from adsorption sites to the precursor state and back at rates characteristic of the local adsorption environment. Since the potential well that binds the precursor molecules to the surface is at most a few kcal/mol deep, their coverage ϑ_p can be assumed small and $d\vartheta_p/dt \rightarrow 0$.^{9,10} The "hopping frequency" for site-to-site diffusion within the deep chemisorption well is large compared to the per site desorption and impingement rates in the measurements,²³ allowing local rearrangement of the adsorbed layer to occur rapidly in response to removal or addition of neighboring molecules. Then, e.g., removal of one molecule from a $c(4 \times 2)$ site to the precursor state allows *on average* $\alpha = \vartheta_{1s}/(\vartheta_{2s} - \vartheta_{1s})$ surrounding molecules to "relax" to the environment characteristic of $c(8 \times 2)$ sites, and return of a precursor molecule to a site surrounded by $c(8 \times 2)$ neighbors causes α of them to be converted to $c(4 \times 2)$, which results in a net addition of $(\alpha + 1)$ $c(4 \times 2)$ molecules. Applying the same logic to interconversion of (2×1) and $c(4 \times 2)$ molecules, with $\beta = \vartheta_{2s}/(\vartheta_{3s} - \vartheta_{2s})$, one obtains the following set of mass balance equations that describe the time-dependent coverages ϑ_1 , ϑ_2 , ϑ_3 , and ϑ_p :

$$\begin{aligned} \frac{d\vartheta_1}{dt} &= k_{p1}\vartheta_p\vartheta_v - k_{1p}\vartheta_1 + \alpha(k_{2p}\vartheta_2 - k_{p2}\vartheta_p\vartheta_1), \\ \frac{d\vartheta_2}{dt} &= (1 + \alpha)(k_{p2}\vartheta_p\vartheta_1 - k_{2p}\vartheta_2) \\ &\quad + \beta(k_{3p}\vartheta_3 - k_{p3}\vartheta_p\vartheta_2), \\ \frac{d\vartheta_3}{dt} &= (1 + \beta)(k_{p3}\vartheta_p\vartheta_2 - k_{3p}\vartheta_3), \\ 0 &= \frac{d\vartheta_p}{dt} = k_{1p}\vartheta_1 - k_{p1}\vartheta_p\vartheta_v + k_{2p}\vartheta_2 - k_{p2}\vartheta_p\vartheta_1 \\ &\quad + k_{3p}\vartheta_3 - k_{p3}\vartheta_p\vartheta_2 + \tau F - k_{pg}\vartheta_p, \quad (1) \end{aligned}$$

where k_{ij} is the rate constant for conversion from state "*i*" to state "*j*," with subscript "*g*" denoting the gas phase; τ is the "trapping probability," i.e., the probability that an impinging gas molecule enters the precursor state; and F is the flux of molecules to the surface (ml/s). Limited coverage ranges can be identified where only two different adsorption environments exist on the surface [e.g., vacancies and $c(8 \times 2)$, $c(8 \times 2)$ and $c(4 \times 2)$, or $c(4 \times 2)$ and (2×1)], allowing Eq. (1) to be reduced to simple functional forms for algebraic comparison to the data of Figs. 4 and 6.

Consider first the data for coverages below about 0.6 ml, where only $c(8 \times 2)$ and empty sites should be present on the surface. In this circumstance, $\vartheta_2 = \vartheta_3 = 0$, $\vartheta_v = (1 - \vartheta_1/\vartheta_{1s})$, and the total surface coverage is $\vartheta = \vartheta_1$. In terms of ϑ , the following result from Eq. (1):

$$r(\vartheta) = \frac{k_{pg}k_{1p}\vartheta}{k_{pg} + k_{p1}(1 - \vartheta/\vartheta_{1s})},$$

$$S(\vartheta) = \frac{\tau k_{p1}(1 - \vartheta/\vartheta_{1s})}{k_{pg} + k_{p1}(1 - \vartheta/\vartheta_{1s})}. \quad (2)$$

The near constancy of $S(\vartheta)$ implies $k_{pg} \ll k_{p1}(1 - \vartheta/\vartheta_{1s})$ in this coverage range, i.e., $S(\vartheta) = \tau$, and equilibrium between the chemisorbed and precursor states is maintained during desorption. In this limit, the expression for the desorption rate can be rearranged to give

$$\frac{r(\vartheta)}{\vartheta} = \frac{r(\vartheta)}{\vartheta_{1s}} + \frac{k_{pg}k_{1p}}{k_{p1}}. \quad (3)$$

Thus, if Eq. (2) and the associated assumptions reflect an accurate description of the adsorption/desorption mechanism, plots of $r(\vartheta)/\vartheta$ vs $r(\vartheta)$ yield straight lines with equal slopes $m = 1/\vartheta_{1s}$ and temperature-dependent intercepts $b = k_{pg}k_{1p}/k_{p1}$, where the ratio k_{1p}/k_{p1} can be recognized as the equilibrium constant for the reaction that yields a precursor molecule and a vacant site from a $c(8 \times 2)$ chemisorbed molecule. Figure 7 shows the data of Fig. 4 arranged according to this prescription, from which $\vartheta_{1s} = 0.68 \pm 0.02$ ml is estimated for the saturation coverage of the $c(8 \times 2)$ structure (cf. 5). An Arrhenius plot of the intercepts, shown in Fig. 8, gives $\nu_{pg}\nu_{1p}/\nu_{p1} = 7.6 \times 10^{14 \pm 0.2} \text{ s}^{-1}$ for the combined preexponential factor and $E_{pg} + E_{1p} - E_{p1} = 31.1 \pm 0.4 \text{ kcal/mol}$ for the combined activation energy, which in this case is the net depth of the chemisorption well. The relatively high precision of these is a consequence of the fact that all the data contribute to the determination of only three parameters and that the collinearity of the points in both plots is excellent. This suggests there is little if any variation of the parameters with coverage and substantiates the viability of the model.

Consider now the desorption data for the coverage re-

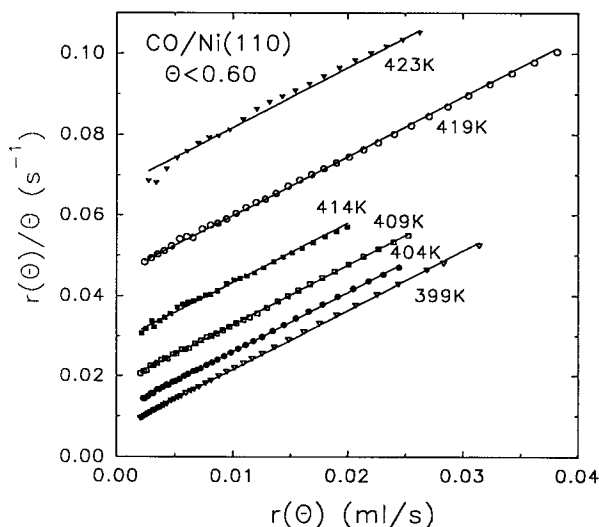


FIG. 7. The desorption rate for $\vartheta < 0.6$ ml plotted according to Eq. (3). Fits to the data are shown as solid lines, the slopes of which give $\vartheta_{1s} = 0.68 \pm 0.02$ ml.

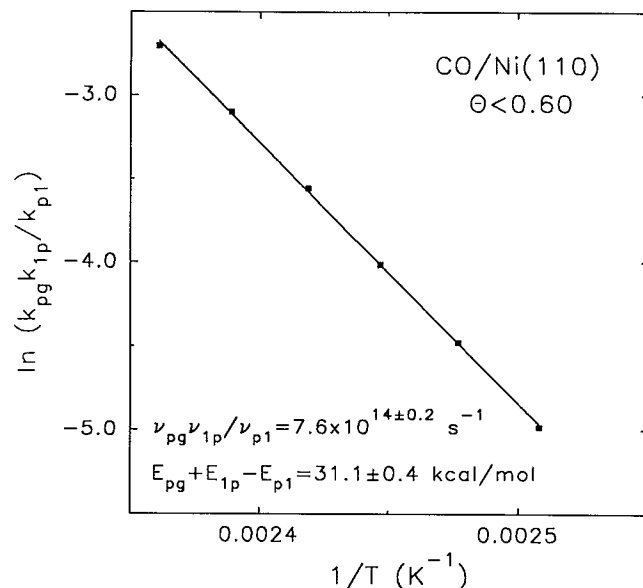


FIG. 8. Arrhenius analysis of the intercepts $k_{pg}k_{1p}/k_{p1}$ from Fig. 7.

gime above about 0.8 ml, where only $c(4 \times 2)$ and (2×1) sites coexist on the surface. Fundamentally different behavior is observed— $r(\vartheta)$ grows almost linearly with coverage, other than a small upturn for $\vartheta > 0.95$ ml. Although the upturn may be a subtle mechanistic feature of the desorption process that is not described by Eq. (1), we suspect it is a measurement artifact (*vide infra*), thus we will ignore it for the analysis that follows. In terms of total surface coverage $\vartheta = \vartheta_2 + \vartheta_3$, the following results from Eq. (1):

$$r(\vartheta) = \frac{k_{pg}k_{3p}(1 + \beta)(\vartheta - \vartheta_{2s})}{k_{pg} + k_{p3}\beta(\vartheta_{3s} - \vartheta)}. \quad (4)$$

The data are consistent with $k_{pg} \gg k_{p3}\beta(\vartheta_{3s} - \vartheta)$, or $r(\vartheta) = k_{3p}(1 + \beta)(\vartheta - \vartheta_{2s})$. In contrast to the behavior evident at low coverages, this indicates that equilibrium between the chemisorbed and precursor states is not achieved during desorption, but would be achieved between the gas phase and the precursor state during adsorption at these temperatures. Fits to the data for this limiting circumstance are shown in Fig. 9, from which $\vartheta_{2s} = 0.78 \pm 0.01$ ml is estimated for the saturation coverage of the $c(4 \times 2)$ overlayer, giving $\alpha \approx 6.8$ and $\beta \approx 3.6$. An Arrhenius plot for k_{3p} , shown in Fig. 10, gives $E_{3p} = 29 \pm 2 \text{ kcal/mol}$ for the activation energy and $\nu_{3p} = 6 \times 10^{16 \pm 1.4} \text{ s}^{-1}$ for the preexponential factor.

The decreased statistical precision of these numbers reflects the particular difficulties associated with isothermal data collection in the limit of saturation coverage. Rapid heating during the temperature step releases unavoidably some CO from the sample holder that can cause a small, transient increase in the $m/e = 28$ amu background signal, and this can contribute adventitiously to the desorption signal, particularly in the first few seconds after the step is completed. Although care was taken to minimize this effect, it could not be completely eliminated. It probably accounts for

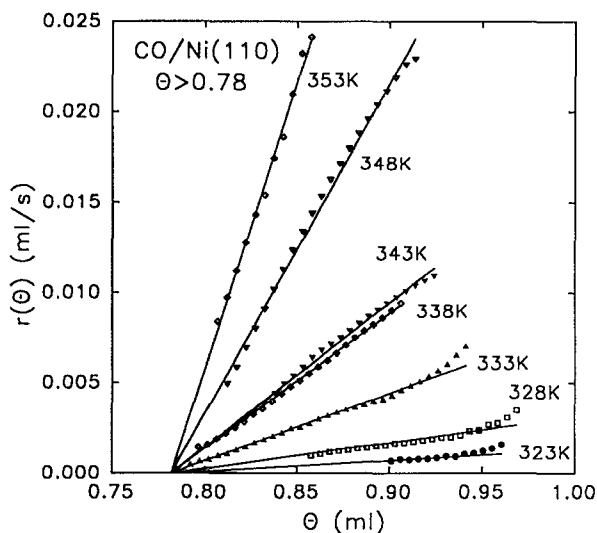


FIG. 9. The desorption rate for high coverages with fits of Eq. (4) shown as solid lines. The intercepts with the ϑ axis give $\vartheta_{2s} = 0.78 \pm 0.01$ ml.

the small upturn in the curves for 323, 328, and 333 K, and it may skew the slopes of some of the curves, particularly at 338 and 343 K, but it does not contribute gross systematic errors to the rate parameters of Fig. 10.

For the adsorption probability in this coverage range, Eq. (1) reduces to

$$S(\vartheta) = \frac{\tau k_{p3} \beta (\vartheta_{3s} - \vartheta)}{k_{pg} + k_{p3} \beta (\vartheta_{3s} - \vartheta)}. \quad (5)$$

The curves for $S(\vartheta)$ indicate that the magnitudes of k_{pg} and $k_{p3} \beta (\vartheta_{3s} - \vartheta)$ are comparable at the lower temperatures of the adsorption measurements. In this circumstance, Eq. (5) can be rearranged to give

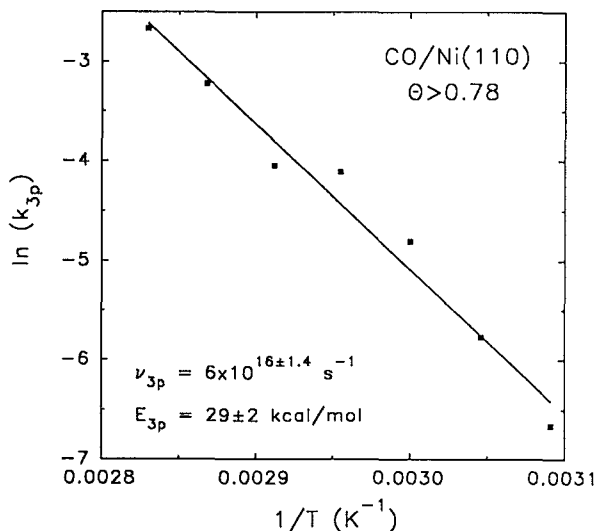


FIG. 10. Arrhenius analysis of k_{3p} values determined from the slopes of Fig. 9.

$$\frac{S(\vartheta)/\tau}{1 - S(\vartheta)/\tau} = \frac{k_{p3}}{k_{pg}} \beta (\vartheta_{3s} - \vartheta). \quad (6)$$

Plots of the data according to this prescription (not shown) with $\tau = 0.95$, $\vartheta_{3s} = 1.0$ ml, and $\beta = 3.6$ are consistent with this functional form, and Arrhenius analysis of the results gives $\nu_{pg}/\nu_{p3} = 1.5 \times 10^{2 \pm 0.5}$ and $E_{pg} - E_{p3} = 1.1 \pm 0.2$ kcal/mol.²² The ratio ν_{pg}/ν_{p3} indicates, as one would expect, that the transition state entropy for motion from the precursor state toward the surface is less than for motion toward the gas phase,^{3,10} and the activation energy difference indicates that the barrier between the precursor and the (2×1) chemisorbed state lies 1.1 kcal/mol below the vacuum level (cf. Fig. 1). The negative of the differential heat of adsorption, i.e., the energy required to convert $(\beta + 1)$ CO molecules in the (2×1) environment to one molecule in the gas phase and β in the $c(4 \times 2)$ environment, is $E_{pg} + E_{3p} - E_{p3} = 30 \pm 2$ kcal/mol.

The values of the saturation coverages estimated from $r(\vartheta)$, $\vartheta_{1s} \approx 0.68$ and $\vartheta_{2s} \approx 0.78$ ml ($\alpha = 6.8, \beta = 3.6$), can be compared to the ideal values $\vartheta_{1s} = 0.625$ and $\vartheta_{2s} = 0.75$ ml ($\alpha = 5, \beta = 3$) determined from the symmetry of the respective LEED patterns and shown in Fig. 2.¹¹ Although the agreement is reasonable, some discrepancy results undoubtedly from failure to fully saturate the surface before each measurement, as has been discussed before for this system.¹³ For example, if we assumed the saturation coverage for the data of Fig. 4 was 0.95 rather than 1.0 ml, we would have estimated $\vartheta_{1s} = 0.65$ and $\vartheta_{2s} = 0.74$ from the preceding analysis, in very good agreement with the ideal values. We proceed to analyze the data with the measured values of ϑ_{1s} and ϑ_{2s} ; use of the ideal values does not compel a different interpretation and causes insignificant changes in the magnitudes of the rate parameters we extract from the data.

The situation for coverages between ϑ_{1s} and ϑ_{2s} is more complicated than the previous cases, since desorption from $c(8 \times 2)$ and $c(4 \times 2)$ sites occurs at comparable rates, as evidenced by the fact that they do not give distinct peaks in TPD.^{11,15,16} In developing an expression for $r(\vartheta)$, we account for desorption from both, but we assume that vacancies created by desorption from $c(8 \times 2)$ sites are filled rapidly by relaxation within the overlayer of neighboring $c(4 \times 2)$ sites, thus no vacancies are available to be filled by precursor molecules returning to the chemisorbed layer, only $c(8 \times 2)$ sites that can be converted to $c(4 \times 2)$. With these assumptions, Eq. (1) yields the following:

$$r(\vartheta) = \frac{k_{pg} k_{1p} \alpha (\vartheta_{2s} - \vartheta) + k_{pg} k_{2p} (1 + \alpha) (\vartheta - \vartheta_{1s})}{k_{pg} + k_{p2} \alpha (\vartheta_{2s} - \vartheta)}, \quad (7)$$

where $\alpha = \vartheta_{1s}/(\vartheta_{2s} - \vartheta_{1s}) = 6.8$ according to the results discussed previously. Equation (7) can be rearranged to give

$$r(\vartheta) = \frac{k_{pg} k_{2p}}{k_{p2}} \left(\frac{1 + \alpha}{\alpha} \right) \left(\frac{\vartheta - \vartheta_{1s}}{\vartheta_{2s} - \vartheta} \right) + \frac{k_{pg} k_{1p}}{k_{p2}} - \frac{r(\vartheta) k_{pg}}{k_{p2} \alpha (\vartheta_{2s} - \vartheta)}. \quad (8)$$

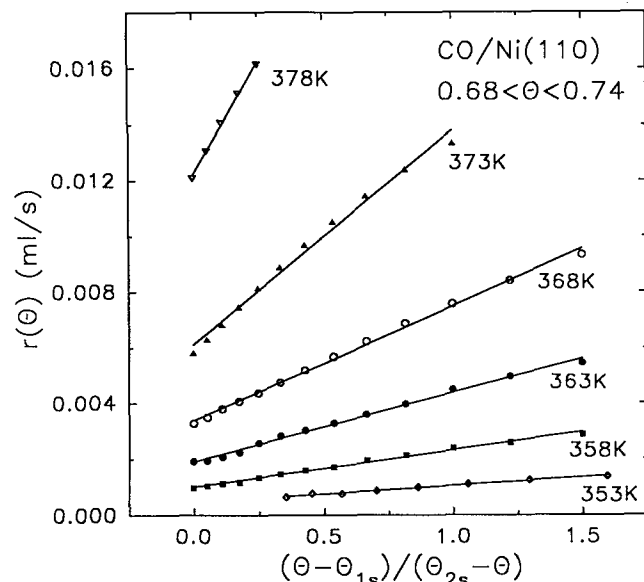


FIG. 11. The desorption rate for $0.68 < \vartheta < 0.74$ plotted according to Eq. (8). The resulting fits are shown as solid lines.

Only as ϑ approaches ϑ_{2s} does the last term make a significant contribution, since $k_{pg} < k_{p2}\alpha(\vartheta_{2s} - \vartheta)$ is implied by the near constancy of the adsorption probability in this coverage range (cf. Fig. 6). Thus isothermal plots of $r(\vartheta)$ vs $(\vartheta - \vartheta_{1s})/(\vartheta_{2s} - \vartheta)$ for $0.68 < \vartheta < 0.74$ ml, as shown in Fig. 11, give straight lines with slopes $m = (k_{pg}k_{2p}/k_{p2})(1 + \alpha)/\alpha$, where the ratio k_{2p}/k_{p2} is the equilibrium constant for the reaction that yields a precursor and α molecules in $c(8 \times 2)$ sites from $(\alpha + 1)$ molecules in $c(4 \times 2)$ sites. An Arrhenius plot of the values for $k_{pg}k_{2p}/k_{p2}$, shown in Fig. 12, gives $E_{pg} + E_{2p} - E_{p2}$

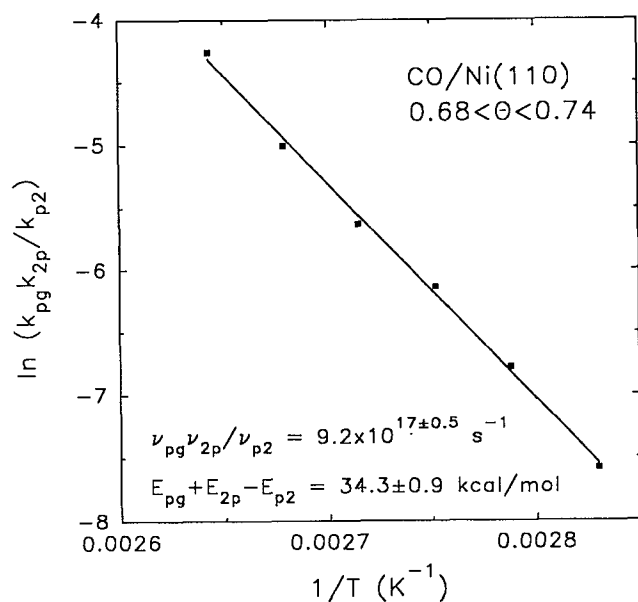


FIG. 12. Arrhenius analysis of $k_{pg}k_{2p}/k_{p2}$ determined from the slopes of Fig. 11.

$= 34.3 \pm 0.9$ kcal/mol for the total energy required to convert $(\alpha + 1) c(4 \times 2)$ molecules to one gas phase and $\alpha c(8 \times 2)$ molecules, and $\nu_{pg}\nu_{2p}/\nu_{p2} = 9.2 \times 10^{17 \pm 0.5} \text{ s}^{-1}$ is obtained for the combined preexponential factor. In the limit $\vartheta \rightarrow \vartheta_{2s}$ or $(\vartheta - \vartheta_{1s})/(\vartheta_{2s} - \vartheta) \rightarrow \infty$, Eqs. (7) and (8) reduce to

$$r(\vartheta \rightarrow \vartheta_{2s}) = \frac{k_{p2}}{k_{pg}} m \alpha (\vartheta_{2s} - \vartheta_{1s}), \quad (9)$$

where m is the slope obtained at lower coverages from Fig. 11. If data for larger values of the abscissa are included in Fig. 11 (not shown), the curves for 353, 358, and 363 K approach asymptotic values from which k_{pg}/k_{p2} can be determined according to Eq. (9). This ratio is near 0.10 for all three, but the narrow temperature range precludes a reliable Arrhenius analysis. If one assumes that the dynamics and energetics of precursor motion to $c(8 \times 2)$ sites to form the $c(4 \times 2)$ state are similar to those for motion to $c(4 \times 2)$ sites to form (2×1) , $\nu_{pg}/\nu_{p2} = \nu_{pg}/\nu_{p3} \approx 150$, and from $k_{pg}/k_{p2} \approx 0.10$ near 350 K, we estimate that the barrier between the precursor and chemisorption wells lies $E_{pg} - E_{p2} \approx 5$ kcal/mol below the vacuum level, which must be close to the depth of the precursor well itself²⁴ and is consistent with the reported instability of a precursor state in this coverage range at 20 K.²⁵ If lower, but still physically reasonable values for ν_{pg}/ν_{p2} are assumed,¹⁰ correspondingly lower estimates for $E_{pg} - E_{p2}$ result, e.g., $\nu_{pg}/\nu_{p2} \approx 10$ gives $E_{pg} - E_{p2} \approx 3$ kcal/mol. Unfortunately, we cannot extract independent values of these two quantities, but can only show that the data are consistent with reasonable combinations of them.

The only rate parameters in Eq. (1) about which we can extract no information from the $r(\vartheta)$ and $S(\vartheta)$ curves are those involving k_{pg}/k_{p1} , the rate constants that describe the relative rates of desorption from the precursor state to the gas phase and chemisorption at vacancies to form $c(8 \times 2)$ sites. This is because no sharp transition in $r(\vartheta)$ or $S(\vartheta)$ occurs near $\vartheta = 0.68$ ml, the coverage at which the $c(8 \times 2)$ state saturates. Nucleation of the $c(4 \times 2)$ state for $\vartheta < 0.68$ ml in adsorption measurements causes $S(\vartheta)$ to remain constant from $\vartheta = 0$ to $\vartheta \approx 0.78$ ml, and desorption from the $c(8 \times 2)$ state begins for $\vartheta > 0.68$ ml [cf. Eq. (7)], where the $c(4 \times 2)$ state is not yet fully depleted. Assuming again that the dynamics of precursor motion to form the chemisorbed state are the same in this coverage range as at higher coverages, we set $\nu_{pg}/\nu_{p1} \approx 150$, and simulations of TPD measurements with this assumption (*vide infra*) lead to an estimate $E_{pg} - E_{p1} \approx 6$ kcal/mol. As before, the assumption of smaller values for ν_{pg}/ν_{p1} would lead directly to lower estimates of $E_{pg} - E_{p1}$.

Table I summarizes this analysis by collecting all of the parameters in Eq. (1) either measured or estimated from the shapes of the $r(\vartheta)$ and $S(\vartheta)$ curves. Since $d\vartheta_p/dt = 0$, ϑ_p can be eliminated from Eq. (1) by solving the last expression for ϑ_p and substituting the result into the previous three. This yields a set of three coupled, nonlinear ordinary differential equations for the coverages $\vartheta_1(t)$, $\vartheta_2(t)$, and $\vartheta_3(t)$, and one can readily verify that Table I includes all the quan-

TABLE I. Summary of parameters determined from $r(\vartheta)$ and $S(\vartheta)$.

Quantity	Magnitude	Description
$c(8 \times 2)$		
ϑ_{1s}	0.68 ± 0.02 ml	From Fig. 7 and Eq. (3)
$\nu_{pg} \nu_{1p} / \nu_{p1}$	$7.6 \times 10^{14 \pm 0.2} \text{ s}^{-1}$	From Fig. 8
$E_{pg} + E_{1p} - E_{p1}$	31.1 ± 0.4 kcal/mol	From Fig. 8
ν_{pg} / ν_{p1}	150	Assumed equal to ν_{pg} / ν_{p3}
$E_{pg} - E_{p1}$	6 kcal/mol	Estimated from TPD simulation
ΔH_1	-31.1 ± 0.4 kcal/mol	Integral heat of adsorption
$c(4 \times 2)$		
ϑ_{2s}	0.78 ± 0.01 ml	From Fig. 9 and Eq. (4)
$\nu_{pg} \nu_{2p} / \nu_{p2}$	$9.2 \times 10^{17 \pm 0.5} \text{ s}^{-1}$	From Fig. 12
$E_{pg} + E_{2p} - E_{p2}$	34.3 ± 0.9 kcal/mol	From Fig. 12
ν_{pg} / ν_{p2}	150	Assumed equal to ν_{pg} / ν_{p3}
$E_{pg} - E_{p2}$	5 kcal/mol	From $k_{pg}/k_{p2} \approx 0.10$ at $T \approx 350$ K
ΔH_2	-31.5 ± 0.6 kcal/mol	Integral heat of adsorption
(2×1)		
ϑ_{3s}	1.0 ml	Assumed
ν_{3p}	$6 \times 10^{16 \pm 1.4} \text{ s}^{-1}$	From Fig. 10
E_{p3}	29 ± 2 kcal/mol	From Fig. 10
ν_{pg} / ν_{p3}	$1.5 \times 10^{2 \pm 0.5}$	From Fig. 6 and Eq. (6)
$E_{pg} - E_{p3}$	1.1 ± 0.2 kcal/mol	From Fig. 6 and Eq. (6)
ΔH_3	-31 ± 1 kcal/mol	Integral heat of adsorption

ties necessary to solve these equations for an arbitrary temperature program $T(t)$ or impinging flux $F(t)$.

IV. DISCUSSION

A. Integral heats of adsorption

An issue of continuing interest is the nature, magnitude, and coverage dependence of interadsorbate interactions in chemisorbed layers. When estimating their magnitudes from desorption rate measurements, it is important to recognize the distinction between the differential heat of adsorption, i.e., the energy change per mole of molecules added to the overlayer at fixed coverage, and the integral heat of adsorption, i.e., the total energy per mole of molecules in the adsorbed layer at fixed coverage.²⁶ It is the integral heat that identifies directly how interadsorbate interactions change with coverage. In this case, desorption has associated with it the relaxation of neighboring molecules in the overlayer to a different local environment, and the energetics of this process must be accounted for when defining the relationship between differential and integral heats of adsorption for each of the (cf. 5) structures.

Since the activation energy for desorption remains constant throughout the coverage range where $c(8 \times 2)$ molecules desorb (cf. Figs. 7 and 8), $\Delta H_1 = -31.1 \pm 0.4$ kcal/mol can be identified as both the differential and integral heat of adsorption of CO in $c(8 \times 2)$ sites. In the intermediate coverage range, the differential heat $-\Delta H = 34.3 \pm 0.9$ kcal/mol includes contributions due to conversion of α $c(4 \times 2)$ molecules to $c(8 \times 2)$ for each $c(4 \times 2)$ molecule

that desorbs, or $\Delta H = \Delta H_2 + \alpha(\Delta H_2 - \Delta H_1)$, where ΔH_2 is the integral heat of adsorption of $c(4 \times 2)$ molecules. One obtains $\Delta H_2 = -31.5 \pm 0.6$ kcal/mol, indicating that $c(4 \times 2)$ sites are energetically stabilized by 0.4 ± 0.2 kcal/mol relative to $c(8 \times 2)$. In terms of near-neighbor pairwise interactions, the compression of the intermolecular spacing from $d \approx 4.0$ Å in the $c(8 \times 2)$ environment to $d \approx 3.7$ Å in the $c(4 \times 2)$ environment contributes an average attraction of $400/6 \approx 70$ cal/mol per CO-CO pair to the total adsorption energy. By similar arguments, $-\Delta H = 30 \pm 2$ kcal/mol in the high coverage regime is related to ΔH_3 , the integral heat of adsorption of (2×1) molecules, by $\Delta H = \Delta H_3 + \beta(\Delta H_3 - \Delta H_2)$, from which $\Delta H_3 = -31 \pm 1$ kcal/mol results. The energetic destabilization of (2×1) with respect to $c(4 \times 2)$ molecules is on the order of 1 kcal/mol, corresponding again to changes in near-neighbor pairwise interactions on the order of 100 cal/mol per CO-CO pair. Note finally that the integral heat of adsorption is constant from zero to saturation coverage to within ± 1 kcal/mol. This comparison shows that relatively small coverage-dependent changes in integral heats of adsorption may be manifested as significantly larger changes in desorption activation energies when relaxation accompanies the adsorption/desorption process.

B. Analysis of preexponential factors

Although the preexponential factors include some statistical uncertainties, one can formulate a scenario on the basis of a few justifiable assumptions that accounts for their

magnitudes with reasonable values of adsorbate partition functions. The success of this analysis, as we will demonstrate, depends critically on the inclusion of the relaxation effect. To see this, consider first the low coverage regime, where molecules desorbing from individual $c(8 \times 2)$ sites leave vacancies, and the magnitude of the combined preexponential is approximately $8 \times 10^{14} \text{ s}^{-1}$ (cf. Fig. 8). According to transition state theory for this circumstance,²⁷

$$\frac{\nu_{pg} \nu_{1p}}{\nu_{p1}} = \kappa \left(\frac{kT}{h} \right) \left(\frac{q_{pg}^{\ddagger}}{q_p} \right) \left(\frac{q_p}{q_1} \right), \quad (10)$$

where κ is the transmission coefficient, q_{pg}^{\ddagger} is the (per site) partition function for the transition state from the precursor to the gas phase, and q_1 is the partition function for molecules chemisorbed in the $c(8 \times 2)$ environment.²⁸ Since the transition state is nearly a free, gas phase molecule, one expects that q_{pg}^{\ddagger} includes contributions due to free rotation, free two-dimensional translation, and C–O vibration, with translational motion perpendicular to the surface removed as the reaction coordinate. The magnitudes of each of these contributions for $T = 350 \text{ K}$, as well as other quantities determined in the ensuing discussion, are summarized in Table II. Assuming these are valid and $\kappa \approx \frac{1}{2}$,⁵ $q_1 \approx 170$ results as the partition function for CO molecules in $c(8 \times 2)$ sites.

In the intermediate coverage regime, the combined preexponential factor $\nu_{pg} \nu_{2p} / \nu_{p2} \approx 9 \times 10^{17} \text{ s}^{-1}$ (cf. Fig. 12) describes relaxation of α molecules from the $c(4 \times 2)$ to the $c(8 \times 2)$ environment for each $c(4 \times 2)$ molecule that desorbs.²⁷ Then

$$\frac{\nu_{pg} \nu_{2p}}{\nu_{p2}} = \kappa \left(\frac{kT}{h} \right) \left(\frac{q_{pg}^{\ddagger}}{q_p} \right) \left(\frac{q_p q_1^{\alpha}}{q_2^{\alpha+1}} \right), \quad (11)$$

and with κ , T , q_{pg}^{\ddagger} , and q_1 as in the previous case, $q_2 \approx 70$ is obtained as the partition function for $c(4 \times 2)$ molecules. The ratio $(q_1/q_2)^{\alpha}$, appearing because of the equilibrium established between the chemisorbed and precursor states, describes the extra contribution of relaxation to the magnitude of the combined preexponential, which is a factor of ≈ 400 in this case. In the temperature range of desorption, the entropy change associated with the decrease from $q_1 \approx 170$ to $q_2 \approx 70$ makes a contribution to the free energy sufficient to outweigh the $\approx 0.4 \text{ kcal/mol}$ energetic stabilization of $c(4 \times 2)$ with respect to $c(8 \times 2)$ molecules, and $c(8 \times 2)$ formation is favored at low coverage. At low temperatures, however, the free energies of the two species are comparable,²⁹ which may explain the onset in low temperature adsorption measurements of $c(4 \times 2)$ formation for $\vartheta < 0.6 \text{ ml}$,¹¹ where vacancies are still available for $c(8 \times 2)$ formation.

In the high coverage regime, where $c(4 \times 2)$ and (2×1) sites (cf. 5) coexist, combining the results of the desorption and adsorption analyses gives $\nu_{pg} \nu_{3p} / \nu_{p3} \approx 9 \times 10^{18} \text{ s}^{-1}$. For this circumstance,

$$\frac{\nu_{pg} \nu_{3p}}{\nu_{p3}} = \kappa \left(\frac{kT}{h} \right) \left(\frac{q_{pg}^{\ddagger}}{q_p} \right) \left(\frac{q_p q_2^{\beta}}{q_3^{\beta+1}} \right), \quad (12)$$

from which $q_3 \approx 10$ is estimated as the partition function for (2×1) molecules. This can be compared with the partition function one calculates on the basis of the measured vibrational spectrum for the (2×1) overlayer.¹⁴ With estimates $\nu_{\text{C-O}} \approx 1900 \text{ cm}^{-1}$ for the C–O stretch, $\nu_{\text{M-CO}} \approx 410 \text{ cm}^{-1}$ for the Ni–CO stretch, $\nu_p \approx 380 \text{ cm}^{-1}$ for two frustrated rotations, and $\nu_{r3} \approx 100 \text{ cm}^{-1}$ for two frustrated translations,

TABLE II. Summary of preexponential factor analysis for $T \approx 350 \text{ K}$.

Quantity	Magnitude	Description
Parameters for transition state theory analysis of preexponential factors		
q_p	130	Partition function for free 2D CO rotation
q_r	280	Partition function for free 2D CO translation, per site basis (Ref. 28)
$q_{\text{C-O}}$	1	Partition function for C–O vibration, $\nu_{\text{C-O}} \approx 1900 \text{ cm}^{-1}$
$q_{pg}^{\ddagger} = q_p q_r q_{\text{C-O}}$	4×10^4	Partition function for transition state, precursor \rightarrow gas phase
κ	$\frac{1}{2}$	Transmission coefficient
kT/h	$7 \times 10^{12} \text{ s}^{-1}$	Transition state frequency factor
Partition functions calculated from preexponential factors		
q_1	170	$c(8 \times 2)$ from Eq. (10)
q_2	70	$c(4 \times 2)$ from Eq. (11)
q_3	10	(2×1) from Eq. (12)
q_{3p}^{\ddagger}	240	Transition state, $(2 \times 1) \rightarrow$ precursor, from Eq. (13)
Vibrational frequencies estimated from partition functions		
$\nu_{\text{C-O}}$	1900 cm^{-1}	C–O stretch (Ref. 14)
$\nu_{\text{M-CO}}$	410 cm^{-1}	M–CO stretch (Ref. 14)
ν_p	380 cm^{-1}	Frustrated rotation ($\times 2$) (Ref. 14)
ν_{r1}	30 cm^{-1}	$c(8 \times 2)$ frustrated translation ($\times 2$) ($q_1 = 170$)
ν_{r2}	40 cm^{-1}	$c(4 \times 2)$ frustrated translation ($\times 2$) ($q_2 = 70$)
ν_{r3}	100 cm^{-1}	(2×1) frustrated translation ($\times 2$) (Ref. 14)

$q_3 \approx 16$ is obtained at 350 K. The discrepancy between the kinetic and spectroscopic estimates is well within the cumulative uncertainties of this analysis. As before, the contribution $(q_2/q_3)^\beta \approx 1100$ due to relaxation of β molecules from (2×1) to $c(4 \times 2)$ is significant, demonstrating that "reasonable" adsorbate partition functions can lead to large values of apparent preexponential factors for desorption when relaxation is evident.

One anticipates that the restoring forces responsible for low frequency, frustrated translational motion of the chemisorbed molecules are most affected by changes of near-neighbor distances in the adsorbed layer. By comparison, the higher frequency stretching motions and the frustrated rotations, associated with the orientative forces that induce preferential chemisorption of CO through the carbon atom, should be less affected, particularly in their contributions to the partition functions.⁵ Assuming the entire increase of $q_1 \approx 170$ and $q_2 \approx 70$ from q_3 can be attributed to changes in the frequency of the two frustrated translations, the frequencies of the other vibrations being identical to those measured for the (2×1) overlayer,¹⁴ $\nu_{r1} \approx 30$ and $\nu_{r2} \approx 40 \text{ cm}^{-1}$ result as estimates for these modes at $c(8 \times 2)$ and $c(4 \times 2)$ sites, respectively. These compare well with frequencies measured by inelastic helium scattering for frustrated translational modes of CO on other surfaces at comparable coverages, $\nu_r = 25\text{--}35 \text{ cm}^{-1}$ on Ni(100) and $\nu_r = 50\text{--}60 \text{ cm}^{-1}$ on Pt(111).³⁰

It is important to recognize that the values of q_1 , q_2 , and q_3 , on which the preceding analysis is based, are specified to higher precision by the data than one might expect. Assuming κ and q_{3p}^\ddagger are the same for all three structures, one can simply take ratios of Eq. (11) to Eq. (10) and Eq. (12) to Eq. (11) to quantify the ratios $(q_1/q_2)^{\alpha+1}$ and $(q_2/q_3)^{\beta+1}$. The cumulative uncertainties in these ratios, as determined by those of the measured preexponential factors, are significant, but the uncertainties in q_1/q_2 and q_2/q_3 are reduced by factors of $\alpha + 1 \approx 7.8$ and $\beta + 1 \approx 4.6$, respectively. The magnitude and uncertainty of $\nu_{pg}\nu_{1p}/\nu_{p1}$ ensure that q_1 is between 150 and 200, and the magnitudes and uncertainties of q_1/q_2 and q_2/q_3 ensure that $q_1 > q_2 > q_3$. These two facts— $150 < q_1 < 200$ and $q_1 > q_2 > q_3$ —are sufficient to make the trends and general conclusions of the preceding analysis robust.

Note finally in this context the significance of $\nu_{3p} \approx 6 \times 10^{16} \text{ s}^{-1}$, the preexponential for motion from (2×1) sites to the precursor state (cf. Fig. 10). Its large magnitude suggests that relaxation of neighboring molecules from (2×1) to $c(4 \times 2)$ sites must be included in the formation of the transition state at the barrier between the chemisorbed and precursor wells. With this assumption, the appropriate expression for ν_{3p} is

$$\nu_{3p} = \kappa \left(\frac{kT}{h} \right) \left(\frac{q_{3p}^\ddagger q_2^\beta}{q_3^{\beta+1}} \right), \quad (13)$$

from which $q_{3p}^\ddagger \approx 240$ results. Since the "corrugation" of the potential energy surface at this point, i.e., its periodic variation parallel to the surface, is weak,³ q_{3p}^\ddagger should include a contribution attributable to nearly free two-dimensional

translation [$q_r = 10\text{--}100$ (Ref. 31)]. With $q_{c-o} = 1$ and vibrational motion perpendicular to the surface being removed as the reaction coordinate, the remaining factor of 2.4–24 in q_{3p}^\ddagger must be attributed to hindered rotation of the transition state. This would suggest that the orientative force for adsorption is significant at the barrier between the precursor and chemisorption wells, which is consistent with scattering measurements of oriented NO beams from Pt(111), where the orientative force is manifested as an increased adsorption probability when NO molecules approach the surface N end first.³²

C. Simulations of other experiments

Since the kinetics analysis differs significantly from any applied previously to this type of problem, it is important that its predictions be checked for consistency when possible by comparison to other experiments.

Consider first a traditional TPD measurement using a linear temperature ramp, i.e., $T(t) = T_0 + \beta t$, where T_0 is the starting temperature and β is the heating rate (K/s). To solve Eq. (1) for this circumstance, we convert the independent variable from t to T via $dt = dT/\beta$; we assume the initial conditions $\vartheta_1 = \vartheta_2 = 0$ and $\vartheta_3 = 1.0 \text{ ml}$ at $T = T_0$; and we integrate the coupled equations numerically with respect to T from $T = T_0$ to $T \rightarrow \infty$ to obtain $\vartheta_1(T)$, $\vartheta_2(T)$, and $\vartheta_3(T)$. The results of this procedure for $T_0 = 80 \text{ K}$ and $\beta = 5 \text{ K/s}$ are shown in the bottom panel of Fig. 13. The

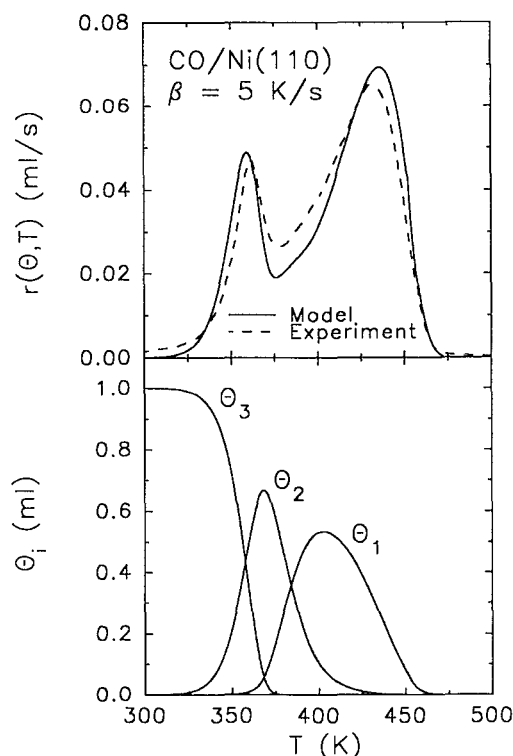


FIG. 13. Simulation of a traditional TPD measurement by solution of Eq. (1) with the rate parameters in Table I and a heating rate of $\beta = 5 \text{ K/s}$. The bottom panel shows the evolution of the coverages of (2×1) (ϑ_3), $c(4 \times 2)$ (ϑ_2), and $c(8 \times 2)$ (ϑ_1) sites as desorption proceeds, and the upper panel compares the total desorption rate from the simulation to a measurement under identical conditions.

total desorption rate $r(\vartheta, T)$ is $-d\vartheta/dT$, where $\vartheta = \vartheta_1 + \vartheta_2 + \vartheta_3$, and this calculation is compared to a TPD experiment for the same conditions in the top panel. The only rate parameter that was varied to optimize the agreement between the TPD curves was $E_{pg} - E_{p1}$, the position below the vacuum level of the barrier between the precursor and the $c(8 \times 2)$ chemisorbed state. The agreement is not perfect, but the simulation accounts very well for the measured peak positions, widths, and heights. Note particularly that the simulation predicts a small change in the slope of $r(\vartheta, T)$ near 400 K on the rising side of the larger peak. This feature, associated with desorption-induced conversion of sites from $c(4 \times 2)$ to $c(8 \times 2)$ symmetry according to our model, is also evident in the measurement and appears in other published TPD data for this system.¹⁵

A question that comes to mind concerns the relationship between the activation energies and preexponential factors in Table I and the "apparent" activation energy $E(\vartheta)$ and preexponential factor $\nu(\vartheta)$ one would measure for this system by more traditional methods of TPD data analysis. To address this issue, we performed a series of simulations for different heating rates, generated isosteric Arrhenius plots for incremental values of the total surface coverage, and analyzed their slopes and intercepts to obtain $E(\vartheta)$ and $\nu(\vartheta)$.³³ The results of this effort, though in good agreement with a similar analysis by others for this system,¹⁶ are surprising and somewhat disconcerting. Only in the limit $\vartheta \rightarrow 0$ does this approach reproduce the parameters we used to calculate the TPD curves. The subtle reason for this can be gleaned from careful inspection of the bottom panel of Fig. 13. Since the temperature is increasing, the rate constants for desorption from each state accelerate as desorption proceeds, causing more than one process to contribute to the overall desorption rate at each value of the total surface coverage. For example, consider the temperature range from 400 to 450 K. The decreasing tail of the curve for ϑ_2 indicates that depletion of $c(4 \times 2)$ sites is contributing to the desorption rate while it is producing $c(8 \times 2)$ sites, and the decrease of the curve for ϑ_1 indicates that desorption from $c(8 \times 2)$ sites is proceeding concurrently to produce vacancies. The relative contributions from these two processes change as the heating rate changes, leading to false values for apparent rate parameters that assume the presence of only one desorption process. This problem appears to be largely obviated when the measurement is performed isothermally. Although we are hesitant to make a general claim on the basis of this single example, we suspect that traditional TPD analyses cannot give reliable estimates of rate parameters for *elementary* desorption reactions in circumstances where multiple, overlapping peaks are evident.³⁴

A straightforward calculation also allows a measurement of $S(\vartheta)$ vs ϑ to be modeled at any temperature. Since the adsorption probability is by definition the ratio of adsorption rate to impinging flux, or $(d\vartheta/dt)/F$, this can be accomplished by dividing the expressions in Eq. (1) by F and integrating them with respect to exposure $\epsilon = Ft$ at constant temperature with $\vartheta_1 = \vartheta_2 = \vartheta_3 = 0$ at $\epsilon = 0$. A curve of $S(\vartheta)$ vs ϑ is generated from this simulation by plotting $d\vartheta/d\epsilon$ vs $\vartheta(\epsilon)$, where $\vartheta = \vartheta_1 + \vartheta_2 + \vartheta_3$. The results of this

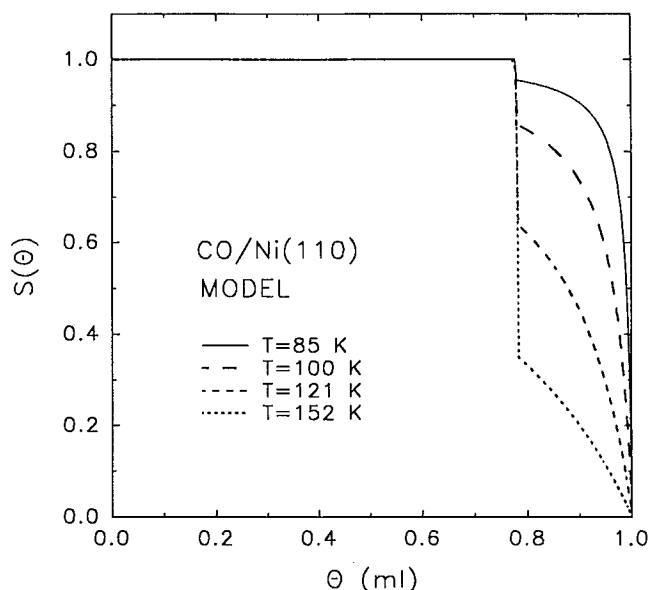


FIG. 14. Simulations of the adsorption probability $S(\vartheta)$ as a function of coverage for $T = 85, 101, 121$, and 152 K. These can be compared directly to the measurements of Fig. 6.

procedure with $\tau = 1.0$ assumed for the trapping probability and $T = 85, 100, 121$, and 152 K are shown in Fig. 14 for direct comparison to the measured $S(\vartheta)/S(\vartheta = 0)$ curves of Fig. 6. The simulations accurately reproduce the region of constant adsorption probability for $\vartheta < \vartheta_{2s}$ ($= 0.78$ ml), the transition near $\vartheta = \vartheta_{2s}$, and the subsequent, temperature-dependent falloff as $\vartheta \rightarrow 1.0$ ml. The only noteworthy discrepancy between the simulations and measurements is the fact that the transition of $S(\vartheta)$ near $\vartheta = 0.78$ ml is spread over a range of approximately 0.10 ml in the measurements, whereas this transition is very sharp in the simulations. Some of the spread is undoubtedly an artifact attributable to measurement statistics, but the remainder most likely results from disorder in the overlayer at low temperatures. Since the model of Eq. (1) assumes perfect relaxation of the overlayer as the coverages of the individual states evolve, an approximation that is clearly better at high than at low temperatures, it cannot account for this effect. To include it would require that the mass balances of Eq. (1) be coupled to equations that describe diffusion within the chemisorbed layer, which is beyond the scope of this analysis.

Another consistency check can be made by comparing the predicted evolution of the coverages in the $c(8 \times 2)$, $c(4 \times 2)$, and (2×1) states during adsorption to measurements of LEED intensities associated with each of these structures, as presented for this system by Behm and co-workers in Ref. 11. Their data for $T = 130$ K show the $c(8 \times 2)$ LEED intensity growing and peaking at an exposure of $\epsilon \approx 2.0$ L.³⁵ As the $c(8 \times 2)$ intensity decays above this exposure, the $c(4 \times 2)$ intensity increases and peaks at $\epsilon \approx 2.5$ L. Finally, the $c(4 \times 2)$ intensity decays as the (2×1)

intensity increases and reaches a constant value near $\epsilon = 4.0$ L. Although the relationship between surface coverage and LEED intensity is complicated by the fact that LEED measures specifically the amplitude of *coherent* scattering from the overlayer,³⁶ the results of many published experiments confirm that maxima in LEED intensities correspond well to maxima in coverages of ordered structures. For comparison, we show in Fig. 15 the coverages ϑ_1 , ϑ_2 , and ϑ_3 as functions of ϵ for a simulation at $T = 121$ K. The general trends and the positions of the maxima in the measurement are reproduced well, but Ref. 11 shows noticeable $c(4 \times 2)$ and (2×1) LEED intensity in the low exposure region preceding the peaks in the $c(8 \times 2)$ and $c(4 \times 2)$ curves. The authors attribute this to some overlap of LEED intensities in the measurements and to formation of $c(4 \times 2)$ and (2×1) islands at low coverage, which is again an effect Eq. (1) is unable to describe.

The satisfactory agreement in these comparisons and the success of the preexponential analysis confirm that the kinetic model is an accurate description of the adsorption/desorption process for this system. However, one should also recognize the limitations of the model in its present form. The only mechanism it provides for converting sites from one type to another is local relaxation during addition or removal of molecules via the precursor state. The partition functions and integral heats of adsorption we extract from the data probably characterize well the thermodynamic state of CO in each of the environments at typical desorption temperatures, but in the absence of a diffusion mechanism to allow site interconversion without adsorption or desorption, the kinetic model cannot describe order/disorder or other thermodynamic phase transformations^{29,37} that may occur within the adlayer as functions of time or time-varying temperature.

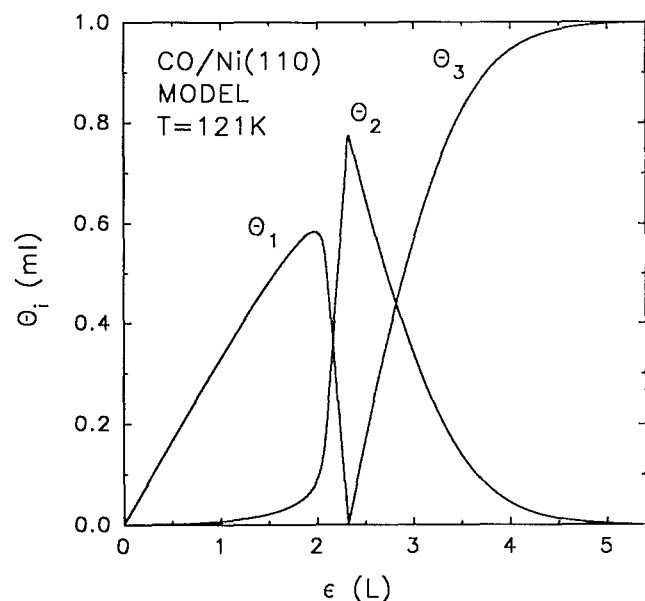


FIG. 15. Evolution of the coverages of (2×1) (ϑ_3), $c(4 \times 2)$ (ϑ_2), and $c(8 \times 2)$ (ϑ_1) sites as a function of exposure at 121 K. These can be compared to the LEED data of Ref. 11.

V. SUMMARY

We have shown that the rate of CO desorption from Ni(110) can be measured under isothermal conditions by programming the sample temperature to approximate a step function. Data collected in this manner can be converted to curves of desorption rate vs coverage for various temperatures, and these, along with measurements of the adsorption probability as a function of coverage, can be rearranged as required for direct, algebraic comparison to the predictions of a mechanistic model of the adsorption/desorption process. A model that includes a precursor at all coverages allows for rate parameters specific to $c(8 \times 2)$, $c(4 \times 2)$, and (2×1) sites and accounts for the relaxation effect depicted in Fig. 2 describes accurately a wide range of rate phenomena, including the structural overlayer evolution of the (cf. 5) as adsorption and desorption proceed. The preexponential factors, when analyzed within the framework of this model, yield partition functions that are consistent with the vibrational spectrum of adsorbed CO, and the activation energies indicate that the integral heat of adsorption for CO remains constant to within 1 kcal/mol between zero and saturation coverage. The formalism we introduce, particularly to account for the important contribution of relaxation to the magnitudes of the adsorption and desorption rate parameters, is likely applicable to many chemisorption systems where several ordered overlayers form as a function of adsorbate coverage.

ACKNOWLEDGMENTS

We thank Bob Carter for his skillful assistance in constructing the apparatus, the NSF for support on Contract Nos. CBT-8808655 and DMR-8818558 (Cornell Materials Science Center), and the Donors of the Petroleum Research Fund, administered by the American Chemical Society.

¹ *Dynamics of Gas-Surface Collisions*, edited by C. T. Rettner and M. N. R. Ashfold (Royal Society of Chemistry, Cambridge, England 1991).

² R. D. Levine and R. B. Bernstein, *Molecular Reaction Dynamics and Chemical Reactivity*, (Oxford University, New York, 1987), Chap. 4.

³ D. J. Doren and J. C. Tully, *Langmuir* **4**, 256 (1988); *J. Chem. Phys.* **94**, 8428 (1991).

⁴ For a cumulative review, see S. L. Lombardo and A. T. Bell, *Surf. Sci. Rep.* **13**, 1 (1991).

⁵ K. J. Laidler, *Chemical Kinetics*, 3rd ed. (Harper and Row, New York, 1987).

⁶ D. King, *Surf. Sci.* **47**, 384 (1975).

⁷ I. Langmuir, *Chem. Rev.* **6**, 451 (1929).

⁸ As described by the authors of Ref. 3, the complex, multidimensional potential energy surface for the adsorbate/adsorbent interaction can be approximated as a one-dimensional function under conditions of thermal equilibrium. This function, known as the "potential of mean force," is the Boltzmann-weighted combination of molecular motions that describes the reaction pathway of minimum energy. The reaction coordinate ξ measures progress along this pathway, and ξ in this case is related, but not necessarily equal to the distance from the surface to the center of mass of the adsorbate molecule.

⁹ R. Gorte and L. D. Schmidt, *Surf. Sci.* **76**, 559 (1978); A. Cassuto and D. A. King, *ibid.* **102**, 388 (1981).

¹⁰ W. H. Weinberg, in *Kinetics of Interface Reactions*, edited by H. J. Kreuzer and M. Grunze (Springer, Heidelberg, 1987), pp. 94-125.

¹¹ R. J. Behm, G. Ertl, and V. Penka, *Surf. Sci.* **160**, 387 (1985).

- ¹² In this context 1 ml = one monolayer = one adsorbate molecule per Ni surface atom, where the surface atom density for Ni(110) is $\sigma = 1.14 \times 10^{19} \text{ m}^{-2}$.
- ¹³ P. R. Norton, P. E. Bindner, and T. E. Jackman, *Surf. Sci.* **175**, 313 (1986).
- ¹⁴ B. Voigtländer, D. Bruchmann, S. Lehwald, and H. Ibach, *Surf. Sci.* **225**, 151 (1990).
- ¹⁵ J. Lee, J. Arias, C. Hanrahan, R. Martin, H. Metiu, C. Clauber, M. D. Alvey, and J. T. Yates, Jr., *Surf. Sci.* **159**, L460 (1985).
- ¹⁶ C. S. Feigerle, S. R. Desai, and S. H. Overbury, *J. Chem. Phys.* **93**, 787 (1990).
- ¹⁷ A. M. Glines, R. N. Carter, and A. B. Anton, *Rev. Sci. Instrum.* **63**, 1826 (1992).
- ¹⁸ M. A. DeAngelis and A. B. Anton, *J. Vac. Sci. Technol. A* (to be published).
- ¹⁹ R. N. Carter and A. B. Anton, *J. Vac. Sci. Technol. A* **10**, 344 (1992).
- ²⁰ C. H. Vincent, *Random Pulse Trains, Their Measurement and Statistical Properties* (Peregrinus, London, 1973), Chap. 4.
- ²¹ G. Comsa and R. David, *Surf. Sci. Rep.* **5**, 145 (1985).
- ²² A. M. Glines, M. A. DeAngelis, and A. B. Anton, *J. Vac. Sci. Technol. A* (in press).
- ²³ The site-to-site hopping frequency is given by $\nu_h \approx 4D\sigma$, where D is the surface diffusion coefficient and σ is the site density [$1.14 \times 10^{19} \text{ m}^{-2}$ for Ni(110)]. R. Gomer, *Rep. Prog. Phys.* **53**, 917 (1990). Measurements of D for CO on Ni(110) are reported in X.-D. Xiao, X. D. Zhu, W. Daum, and Y. R. Shen, *Phys. Rev. Lett.* **66**, 2352 (1991). At $T = 85 \text{ K}$, $\nu_h > 10 \text{ s}^{-1}$, whereas the per site impingement rate in the adsorption measurements is less than 0.01 s^{-1} , and at $T = 350 \text{ K}$, $\nu_h > 10^5 \text{ s}^{-1}$, whereas the per site desorption rate is less than 0.1 s^{-1} .
- ²⁴ Similar behavior has been reported for the interaction of CO with Ni(100) in the limit of zero coverage. M. P. D'Evelyn, H.-P. Steinrück, and R. J. Madix, *Surf. Sci.* **180**, 47 (1987).
- ²⁵ Y. Hsu, K. Jacobi, and H. H. Rotermund, *Surf. Sci.* **117**, 581 (1982).
- ²⁶ A. W. Adamson, *Physical Chemistry of Surfaces*, 4th ed (Wiley, New York, 1987), p. 560.
- ²⁷ A. B. Anton, *J. Phys. Chem.* (to be published).
- ²⁸ Since coverages are expressed in monolayers, the translational partition functions are normalized to $\sigma^{-1} = 8.8 \times 10^{-20} \text{ m}^2$, the area of a unit cell on the Ni(110) surface. Also, activation energies are referenced to the zero points of the potential wells, thus the vibrational partition functions do not include zero-point contributions. W. H. Weinberg, *Dynamics of Gas-Surface Collisions*, pp. 171–220. In principle, the adsorbate partition functions should account for changes in the vibrational spectrum of the adsorbent surface, but this effect does not seem to be important for CO on Ni(110). E. G. Seebauer, A. C. F. Kong, and L. D. Schmidt, *Surf. Sci.* **193**, 417 (1988).
- ²⁹ M. A. DeAngelis and A. B. Anton (to be published).
- ³⁰ R. Berndt, J. P. Toennies, and C. Wöll, *J. Electron. Spectrosc. Relat. Phenom.* **44**, 183 (1987).
- ³¹ A. Clark, *Theory of Adsorption and Catalysis* (Academic, New York, 1970), pp. 57–60.
- ³² E. W. Kuipers, M. G. Tenner, A. W. Kleyn, and S. Stolte, *Phys. Rev. Lett.* **62**, 2152 (1989).
- ³³ J. L. Taylor and W. H. Weinberg, *Surf. Sci.* **78**, 259 (1978).
- ³⁴ We are currently investigating the generality of this phenomenon. K. J. Lyons and A. B. Anton (to be published).
- ³⁵ $1 \text{ L} = 1 \text{ Langmuir} = 1.0 \times 10^{-6} \text{ Torr s}$.
- ³⁶ *Determination of Surface Structure by LEED*, edited by P. M. Marcus and F. Jona (Plenum, New York, 1984).
- ³⁷ E. Bauer, in *Structure and Dynamics of Surfaces II*, edited by W. Schommers and P. von Blanckenhagen (Springer, Berlin, 1987), pp. 115–179.